Astronomy
&
Astrophysics

Stellar population gradients in bulges along the Hubble sequence[*],[**]

I. The data

J. Gorgas[1], P. Jablonka[2], and P. Goudfrooij[3]

[1] Dpto. de Astrofísica, Facultad de Físicas, Universidad Complutense de Madrid, 28040 Madrid, Spain
[2] Observatoire de l'Université de Genève, Laboratoire d'Astrophysique de l'École Polytechnique Fédérale de Lausanne (EPFL), 1290 Sauverny, Switzerland
  e-mail: `pascale.jablonka@obs.unige.ch`
[3] Space Telescope Science Institute, 3700 San Martin Drive, Baltimore, MD 21218, USA

ABSTRACT

This is the first paper presenting our long-term project aimed at studying the nature of bulges through analyzing their stellar population gradients. We present deep spectroscopic observations along the minor axis and the data reduction for a sample of 32 bulges of edge-on spiral galaxies. We explain in detail our procedures for measuring their dynamical parameters (rotation curves and velocity dispersion profiles) and line-strength indices, including the conversion to the Lick/IDS system. Tables giving the values of the dynamical parameters and line-strength indices at each galactocentric radius are presented (in electronic form) for each galaxy of the sample. The derived line-strength gradients from this dataset will be analyzed in a forthcoming paper to set constraints on the different scenarios for the formation of the bulges.

Key words. galaxies: bulges – galaxies: stellar content – methods: data analysis – galaxies: abundances – galaxies: evolution – galaxies: formation.

1. Introduction

Bulges of spiral galaxies are cornerstones for constraining theories of galaxy formation. Located at the centers of spiral galaxies, they hold the signature for the sequence of formation of the different sub-systems building a spiral galaxy: halo, disk, and bulge. While the mass of disks of spiral galaxies in the local universe is approximately constant among spirals of different Hubble types (e.g., Arimoto & Jablonka 1991), the prominence of bulges varies widely along the Hubble sequence. Hence, bulges are likely to hold important clues to our understanding of galaxy evolution and the nature of the Hubble sequence.

Formation scenarios for bulges can be divided into two categories. One of them states that bulges are formed in a similar way to low- to intermediate-mass elliptical galaxies, based on the strong similarities between the global properties of many bulges and of elliptical galaxies. Bulges and (small) ellipticals populate the same location in the fundamental plane (Bender et al. 1992; Falcón-Barroso et al. 2002), and they form a continuous sequence in the $V_{\max}/\sigma$ vs. ellipticity diagram (being supported by rotation; Bender et al. 1992). Furthermore, spectroscopic studies of the central part of bulges have shown that their mass-metallicity relation (when derived from α elements, e.g. the Mg_2 index) is consistent with the relation found for

elliptical galaxies (Jablonka et al. 1996; Idiart et al. 1996; Moorthy & Holtzman 2006), but see also Prugniel, Maubon, & Simien (2001) and Proctor & Sansom (2002). We refer the reader to the introduction in Jablonka et al. (2007, hereafter Paper II) for a discussion of previous spectroscopic studies of bulges.

The other popular type of formation scenario for bulges is the "secular evolution" scenario in which bulges form from disk material through redistribution of angular momentum. This scenario involves stellar bars driving gas from the disk into the central region of the galaxy, thus triggering star formation (e.g., Pfenniger & Norman 1990; Norman et al. 1996; Kormendy & Kennicutt 2004). If enough mass is accreted, the bar itself will dissolve, and the orbits of stars involved in the process will yield a bulge-like spatial distribution. Galaxies would thus evolve from late to earlier types along the Hubble sequence. Observational support for secular evolution has been provided mainly for late-type spiral galaxies (~Sb and later), including correlations between the scale lengths of bulges and disks (Courteau et al. 1996; McArthur et al. 2003) and the radial light distribution of bulges of late-type spirals being closer to exponential than to classical de Vaucouleurs $R^{1/4}$ profiles (Balcells et al. 2003; de Jong et al. 2004).

Stellar population studies should be able to place important constraints on the formation mechanisms for bulges. If bulges form mainly through dissipative collapse without significant subsequent merging, simulations indicate that the slope of radial metallicity gradients should steepen with increasing galaxy mass and luminosity (Carlberg 1984). Simulations of dissipative merging of gas-rich disks has also been shown to produce

---

[*] Based on observations collected at the Roque de los Muchachos Observatory and at the European Southern Observatory, proposal numbers 58.A-0192(A), 59.A-0774(A) and 61.A-0326(A).
[**] 2 datasets are only available in electronic form at the CDS via anonymous ftp to `cdsarc.u-strasbg.fr` (130.79.128.5) or via `http://cdsweb.u-strasbg.fr/cgi-bin/qcat?J/A+A/474/1081`

metallicity gradients that steepen with increasing mass (e.g., Bekki & Shioya 1999). Conversely, the impact of secular evolution on population gradients is expected to be rather different. Simulations including gas and effects of star formation show that disk gas fueled to the central regions renders a central region that is younger and more metal rich than the outer regions, whereas metallicity gradients outside the central region flatten out significantly ∼1 Gyr after formation of a bar, both for gas and stars (Friedli et al. 1994; Friedli 1998). Observational evidence for this effect exists, albeit so far only for the gas component in spiral disks. Several studies have shown that global radial gradients of the gas metallicity in barred spirals are shallower than gradients in unbarred spirals of the same Hubble type (Vila-Costas & Edmunds 1992; Zaritsky et al. 1994; Martin & Roy 1994).

In terms of *stellar* population gradients in bulges, past studies have mainly used broad-band imaging. The studies of Balcells & Peletier (1994) and Peletier et al. (1999) used optical and near-infrared colors and found that color gradients of luminous bulges increase with luminosity, whereas faint bulges show stronger gradients than expected from the trend observed for the luminous bulges. However, information in colors is generally rather degenerate in age, metallicity, and/or extinction.

Spectroscopic studies allow the measurement of line strength indices that are insensitive to dust extinction and allow a cleaner separation of age and metallicity of a stellar population. While line strength gradients have been measured for many elliptical and S0 galaxies using the Lick/IDS system of indices (e.g., Carollo et al. 1993; González & Gorgas 1996; Fisher et al. 1996; Mehlert et al. 2003; Kuntschner et al. 2006; Sánchez-Blázquez et al. 2006a), such data are relatively hard to acquire for bulges of spirals at high enough signal-to-noise ratios, given the often low surface brightness of bulges and the difficulty of disentangling the observed spectra into bulge and disk components. This is especially difficult for late-type spirals in face-on or moderately inclined configurations.

With this in mind, we embarked on an extensive spectroscopic survey of 32 spiral galaxies in an edge-on configuration to avoid contamination by disk light and with Hubble types ranging from S0 to Sc. Early results from subsets of the data acquired during this survey were published in Goudfrooij et al. (1999), Jablonka et al. (2002), and Gorgas et al. (2003). In this first paper on the final and comprehensive results of this survey, we present the extensive data reduction and analysis procedures leading to the final line strength measurements. The galaxy sample is presented in Sect. 2. Section 3 describes the observations, and Sect. 4 provides details on the data reduction procedures. Section 5 contains a description of the determination of dynamical parameters (radial velocities and velocity dispersions as a function of bulge radius), and the line strength index measurements themselves are described in Sect. 6. Finally, Sect. 7 contains a summary of this work.

2. The sample

We selected a sample of 32 genuine (or close to) edge-on spiral galaxies. Galaxies in the northern hemisphere were selected from the Uppsala General Catalogue (Nilson 1973), while southern galaxies were selected from the ESO/Uppsala catalogue (Lauberts 1982). As shown in Fig. 1, the galaxies span a wide range in Hubble types (from S0 to Sc). Given the edge-on configuration of the galaxies, precise morphological classification is difficult. Due to this we considered a Hubble T-type uncertainty of ±1, which is also a fair representation of the catalogue-to-catalogue variations for a given galaxy.
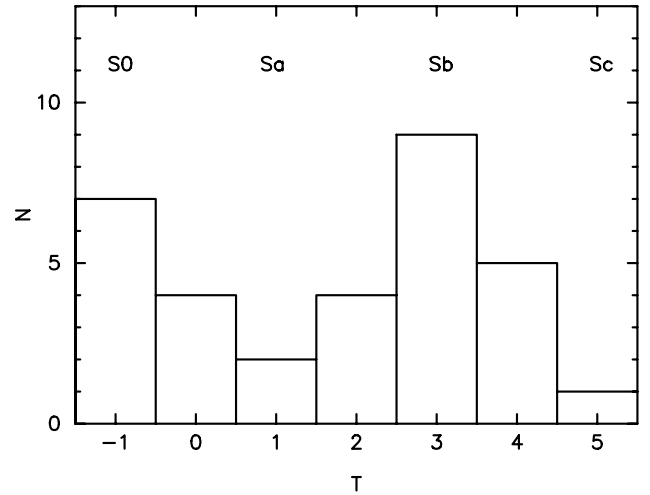

Fig. 1. Histogram showing the distribution in Hubble types of the galaxy sample.

All the galaxies are nearby objects, with radial velocities between 550 and 6200 km s^{-1}, and were chosen to cover a range in bulge luminosity ($-17.5 > M_V > -20.5$). Table 1 lists the galaxy sample and some relevant parameters, including the corresponding bulge types (from Lütticke et al. 2000) and the local environment, which also varies significantly among the sample galaxies. A few galaxies have previous photometric and spectroscopic observations from other authors (see Sect. 6) and were included for comparison purposes.

3. Spectroscopic observations

Spectroscopic observations of the galaxy sample were obtained during five observing runs at three different telescopes: The northern galaxies were observed at the 2.5-m Isaac Newton Telescope (INT) of the Isaac Newton Group of telescopes on the island of La Palma (Spain). For the southern galaxies, we used the 3.6-m ESO telescope and 3.6-m New Technology Telescope (NTT), both at ESO La Silla observatory (Chile). The main parameters of the instrument configurations and other details of the observing runs are listed in Table 2. Using slit widths from 1.0 to 2.0 arcsec, the different spectrographs allowed us to obtain spectra at a resolution of typically 4 Å (*FWHM*, as measured from the widths of arc lines), except for run 3 (the ESO 3.6-m run), where a resolution of 8.3 Å was attained. The spectral range from around λ3900 Å to λ5500 Å (with the exception of the ESO NTT runs, in which the spectra extended redward to λ6650 Å), was chosen to include the main prominent spectral features of the blue-yellow spectra of the galaxies, in particular most of the Lick/IDS line-strength indices.

Table 1 includes some relevant observational parameters for the galaxy sample. The spectrograph slit was oriented along the minor axis of the bulges. Thus, effects of contamination by disk light are only expected for the very central regions of the sample galaxies. Exposure times ranged from 1.5 to 5 h per galaxy, providing high signal-to-noise (S/N) spectra out to the outer regions of most bulges. We obtained reliable spectra out to the effective radius (r_{eff}) for every galaxy in our sample. Furthermore, our spectra reached $S/N > 10$ (per Å and per arcsec in the spatial direction) beyond $2r_{eff}$ for 80% of the sample galaxies. Some observations of nearby bulges were especially deep, providing useful spectra out to several kpc from the centers of the bulges

Table 1. The galaxy sample.

	Type	T	B_{T}	i	Bulge type[a]	Environment	Run[b]	PA[c]	Exp.[d]	r_{eff}^e	Δr_{eff}	$V_{\max}^f$
NGC 522	Sc	4.1	13.98	90	box		2	123	8200	3.5	0.7	196.1
NGC 585	Sa	1.0	14.06	90	close to box		4,5	86	7200	2.4	0.7	246.6
NGC 678	SBb	3.0	13.31	90	box	cluster	1	168	12 000	23.3	1.4	169.0
NGC 891	SAb	3.0	10.83	88	box		1	112	10 500	13.2	0.7	212.0
NGC 973	Sbc	3.2	14.17	90	box		2	138	13 800	3.4	0.4	270.0
NGC 1032	S0-a	0.4	12.74	90	elliptical	companions?	1	158	9000	11.4	1.1	283.9
NGC 1184	S0-a	0.0	12.95	90	close to box		2	79	8200	11.3	1.9	
NGC 1351A	SBbc	4.5	14.16	80	elliptical	cluster	5	132	5400	5.8	0.8	90.7
NGC 1886	Sab	3.9	13.80	90	peanut	isolated	3	60	10 800	1.6	0.3	154.6
NGC 3957	SA0	−1.0	13.03	90	close to box	cluster	3	173	7200	4.0	0.8	
NGC 5084	S0	−1.8	11.55	90	elliptical	cluster	3	80	7200	38.1	11.6	310.3
NGC 6010	S0-a	0.4	12.95	90			1	15	13 800	4.2	0.9	148.8
NGC 6829	Sb	3.0	15.09	90			2	121	12 800	7.1	1.4	211.9
NGC 7183	S0	−0.7	13.14	90	close to box		5	77	7200	2.5	0.5	209.9
NGC 7264	Sb	3.1	14.58	90	elliptical		2	147	13 000	1.2	0.4	248.0
NGC 7332	S0	−2.0	12.56	90	close to box		1	65	15 000	7.5	1.1	121.3
NGC 7396	Sa	1.0	13.85	60	elliptical		2	13	13 000	25.2	1.6	360.7
NGC 7703	S0	−2.0	14.41	90	elliptical	cluster	2	57	6400	4.8	2.0	159.5
NGC 7814	SAab	2.0	11.68	67	elliptical		1	45	18 400	33.5	2.0	231.0
IC 1711	Sb	3.0	14.53	90	elliptical		2	133	6200	2.1	0.5	173.4
IC 1970	SAb	3.1	13.36	88	elliptical		4	75	7200	8.1	1.0	118.9
IC 2531	Sb	4.9	12.88	90	peanut	cluster	3	75	7200	2.3	0.3	228.1
IC 5176	SABbc	4.4	13.02	90	elliptical	companions?	5	151	7200	4.6	0.3	164.2
IC 5264	Sab	2.3	13.58	90	elliptical	group	4,5	82	12 600	2.8	0.1	230.6
UGC 10043	Sbc	4.1	15.17	90		cluster	2	61	12 200	1.0	0.3	143.6
UGC 11552	Sab	2.0	15.68	75			5	16	7200	11.7	0.6	243.0
UGC 11587	S0	−1.9	14.52	90			1	76	15 000	5.7	0.7	
ESO 079-003	SBb	3.1	13.91	90	close to box		4,5	134	10 800	5.9	2.0	192.2
ESO 234-053	S0	−1.9	14.32	90			5	81	5400	1.7	0.1	
ESO 311-012	S0-a	0.1	12.38	90	box	isolated	3	14	7200	7.4	1.3	95.9
ESO 443-042	Sb	3.1	13.85	90	peanut	companions?	3	130	10 800	3.8	0.7	166.3
ESO 512-012	Sbc	3.2	14.42	90	peanut		3	113	5400	1.4	0.3	224.9

[a] From Lütticke et al. (2000). [b] Run number in which each galaxy was observed. [c] Position angle of the long slit. [d] Total exposure time (in seconds). [e] Effective radius (in arcseconds) of the bulge, computed as explained in Sect. 4. [f] Maximum rotational velocity (in km s^{-1}) along the disk major axis, corrected from inclination when necessary. Hubble type T, total apparent magnitude B_{T}, galaxy inclination i and $V_{\max}$ have been taken from HyperLeda (http://leda.univ-lyon1.fr/).

(e.g., ∼7 kpc for NGC 5084 and ∼4 kpc for NGC 7814). In the central regions we obtained spectra with S/N ranging from 20 to 240, depending, among other factors, on the obscuration by dust lanes within the galaxy disk.

In each observing run we also acquired spectra of a number of template stars from the Lick/IDS library (Worthey et al. 1994) for calibration purposes (see below), as well as several spectrophotometric standards to calibrate the spectra in flux.

4. Data reduction

The reduction of the data was performed with the REDm$_{\mathrm{m}}^{\mathrm{uc}}$E[1] package (Cardiel 1999). We carried out a standard reduction procedure for spectroscopic data: bias and dark subtraction, cosmic ray cleaning, flat-fielding (using observations of tungsten lamps and twilight skies to correct from high and low frequency variations respectively), C-distortion correction, wavelength calibration, S-distortion correction and recentering of the spectra, sky subtraction, atmospheric and interstellar extinction correction, relative flux calibration, and spectrum extraction. REDm$_{\mathrm{m}}^{\mathrm{uc}}$E is a package specifically written to reduce long-slit spectroscopic observation. Its main advantage is that, for each observed data

frame (including calibration ones), it creates an associated error frame at the beginning of the reduction procedure. From this point, error and data frames are processed in parallel, translating all the uncertainties in the manipulation of the data into the error frames, hence providing very accurate estimates of the random errors associated with the final spectra (see Cardiel et al. 1998).

Although most of the reduction steps were performed using standard procedures for long-slit reduction, we give below some comments on steps of particular importance:

(i) Wavelength calibration

Spectra were converted to a linear wavelength scale using about 90 arc lines fitted by 5th to 7th-order polynomials. The rms dispersion of the fitted position of arc lines was typically 0.25–0.30 Å.

(ii) Spectral rectification and centering

As usual with CCD spectrographs, the galaxy spectra were not perfectly aligned with the detector rows. To correct for this effect (which is crucial when measuring line-strength gradients), we fitted a Cauchy function to the number of counts in a spatial interval around the location of maximum counts for each spectral resolution element, hence determining the position of the galaxy center as a function of wavelength. In galaxies with dust lanes obscuring the light of the central region of the bulge, these central parts were masked when fitting the luminosity profiles. Experiments with galaxies without dust lanes showed that we

---

[1] http://www.ucm.es/info/Astrof/software/reduceme/reduceme.html

Table 2. Instrumental details of the observing runs.

Run	Dates	Telescope	Instrument	Dispersion Å/pixel	Spectral range Å	Slit width arcsec	$FWHM^a$ Å
1	13/08/96–16/08/96	INT 2.5 m	IDS	1.6	3908–5535	2.0	3.9
2	31/08/97–03/09/97	INT 2.5 m	IDS	1.6	3908–5535	2.0	4.3
3	08/03/97–11/03/97	ESO 3.6 m	EFOSC	3.4	3776–5504	1.5	8.3
4	23/09/97–25/09/97	NTT 3.6 m	EMMI	1.3	3971–6649	1.0	3.7
5	23/08/98–26/08/98	NTT 3.6 m	EMMI	1.3	3985–6649	1.5	4.9

^{a} Spectral resolution as measured from arc lines.

could still trace the position of the galaxy center. The resulting map was then fitted by a low-order polynomial, which was in turn used to straighten the spectra. As a result of this process, the central spectrum of the galaxy is moved to the center of a detector row so that symmetric spectra on each side of that row correspond to the same galactocentric radius.

(iii) Sky subtraction

Accurate sky subtraction is critical for studies like this, since we aim to analyze spectra at light levels corresponding to only a few per cent of the sky signal. We refer the reader to Cardiel et al. (1995) for a description of the sky subtraction effects on the measurements of line-strength indices. For each of our galaxy observations we generated a sky image by fitting, for each pixel in the wavelength direction, a low-order polynomial using the regions close to the slit ends. In most cases, the galaxies fill only a small region of the slit, so this synthetic sky image is free of contamination from the galaxy light. However, this is not the case for some of the larger galaxies of the sample (like NGC 7814 and NGC 5084). In these cases, we fitted de Vaucouleurs' $r^{1/4}$ profiles to the surface brightness distribution of the galaxies along the slit, estimating the relative contribution of the galaxy to the regions from where the sky was extracted. We then "decontaminated" the sky frames by subtracting scaled and averaged galaxy spectra. To assess the quality of the sky subtraction, we looked for residuals due to sky emission lines, making sure that they were completely removed, even in the outer parts of the more extended galaxies.

(iv) Measurement of effective radii

Effective radii for all the bulges of the sample were measured by fitting de Vaucouleurs' profiles to the radial surface brightness profiles determined by collapsing the spectra in the wavelength direction. The central regions, affected in many cases by dust lanes, were removed from the fit. In any case, we never used spectra at radii typically below 2 arcsec. On the other hand, the fits were quite insensitive to the outer radius cutoff, although deviations of the luminosity profiles from a straight line in the logarithmic plots were sometimes observed. The derived effective radii are listed in Table 1. The associated errors, in the last column, reflect the sensitivity of the derived radii to the particular choice of the region to be fitted. Note that we are not assuming that the bulges do follow a de Vaucouleurs luminosity profile. (A Sersic profile with an exponent n closer to 1 provides a better fit in many cases, see Andreakis et al. 1995.) However, the derived effective radii provide us with a well-defined parameter to express the line-strength gradients (Paper II) on a homogeneous spatial scale.

(v) Flux calibration

Relative flux calibration of the spectra was achieved using exposures of spectrophotometric standards from Massey et al. (1988), Oke (1990), and Hamuy et al. (1994). In each run we took several repeated observations of 4, 5, 4, 3, and 3 stars (for runs 1 to 5 respectively). In some cases we obtained exposures at
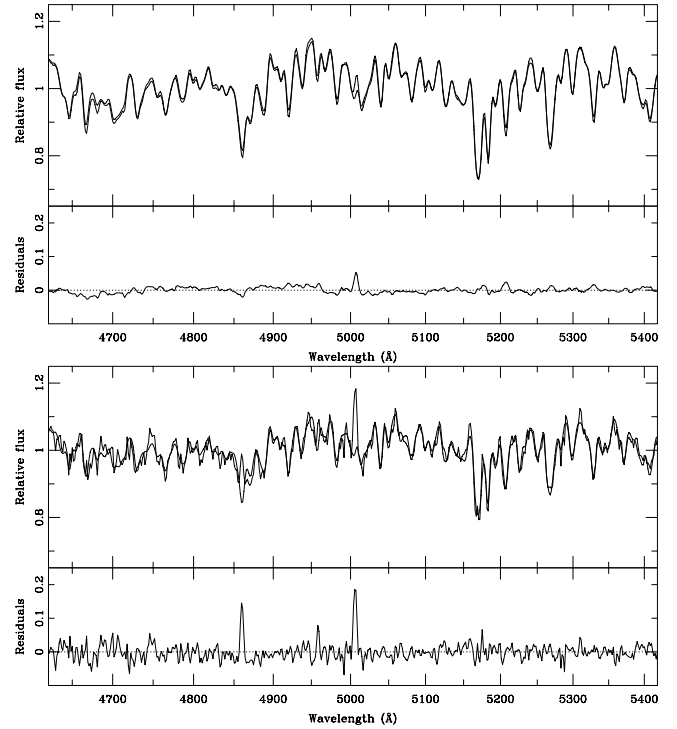

Fig. 2. Illustration of the velocity dispersion determinations using optimal templates for NGC 7332 (*upper plot*) and UGC 10043 (*lower plot*). For each plot, *the upper panels* show the observed galaxy spectrum (thick line) and the corrected optimal template spectrum (thin line). The residuals of the fits are shown in *the lower panels*.

different zenithal distances to check the atmospheric extinction correction. All the calibration curves of each run were averaged, and the flux calibration errors were estimated by the differences among the indices measured with different curves.

(vi) Extraction of spectra

Once the galaxy frames were fully reduced, we added all the frames of the same galaxies and extracted individual spectra along the slit. The availability of reliable error frames allowed us to compute the number of spatial bins to be coadded to guarantee a minimum S/N in the final spectra. Using the prescriptions given in Cardiel et al. (1998), we chose a lower S/N cutoff of 15 (per Å; mean value along the full spectral range), which ensures a typical error in most of the atomic Lick indices below 20%. For the outer spatial regions, we coadded some other spectra to get a minimum S/N of 10, which is enough to measure molecular indices (like Mg_2) with a relative uncertainty below 10%, even though it does lead to significant errors in the atomic indices.

Table 3. Dynamical parameters of the bulge sample.

Galaxy	V_r^a	ΔV_r	V_{rot}^b	ΔV_{rot}	σ_0^c	$\Delta\sigma_0$	$\langle\sigma\rangle^d$	$\Delta\langle\sigma\rangle$	σ_{max}^e	σ_{ref}	Ref^f
NGC 522	2719.0	12.5	12.1	4.9	82.1	9.3	88.2	8.8	99		
NGC 585	5358.4	6.8	5.5	4.5			174.3	4.7	188		
NGC 678	2814.9	15.0	13.3	6.3	163.4	2.1	170.7	4.1	183		
NGC 891	548.2	12.3	1.9	2.2			95.4	5.1	95	72	(2)
NGC 973	4081.0	9.6	1.5	6.0			173.3	9.3	226		
NGC 1032	2702.9	7.7	16.3	9.4			214.2	2.8	225		
NGC 1184	2278.2	8.0	5.1	3.1	230.3	3.0	219.6	7.6	234	229	(3)
NGC 1351A	1329.3	17.6	6.1	15.4			141.4	28.5	141		
NGC 1886	1689.8	15.1	8.0	3.3			111.0	6.5	120		
NGC 3957	1589.7	10.2	1.6	2.2			131.4	5.3	149		
NGC 5084	1671.6	16.8	10.5	9.5	207.6	1.7	200.0	4.0	214	215	(1)
NGC 6010	2058.5	3.3	2.9	3.3	148.4	1.2	146.7	4.9	157	144	(4)
NGC 6829	3303.3	11.0	1.2	5.6			118.1	6.3	130		
NGC 7183	2594.9	12.8	2.2	5.0			138.8	5.3	157		
NGC 7264	4210.1	14.4	6.9	4.6			165.6	6.9	205		
NGC 7332	1206.3	2.2	2.6	2.8	117.2	0.6	116.1	2.8	122	134	(1)
NGC 7396	4882.5	12.2	8.9	6.6			220.6	4.1	224		
NGC 7703	3970.5	7.1	7.1	4.8	149.9	3.2	148.5	5.9	154	166	(3)
NGC 7814	1051.4	6.9	4.8	4.5			170.3	2.4	187	172	(1)
IC 1711	2785.2	11.8	9.0	5.2			122.3	12.2	161		
IC 1970	1300.8	7.2	11.6	10.6			82.8	12.1	95		
IC 2531	2386.8	11.7	3.8	4.1			126.6	8.7	127		
IC 5176	1739.3	10.5	4.1	4.3			152.7	6.4	160		
IC 5264	2025.1	6.3	2.6	3.6			101.1	3.4	106		
UGC 10043	2180.3	16.0	8.2	6.4			88.5	15.7	89		
UGC 11552	4479.5	11.1	2.7	11.3			151.3	10.7	167		
UGC 11587	4481.5	7.8	2.3	4.9	213.0	2.9	203.4	8.5	224		
ESO 079-003	2613.5	8.1	1.5	6.8			120.7	8.5	160		
ESO 234-053	6232.9	16.0	0.3	4.9	204.9	3.1	200.4	7.6	226		
ESO 311-012	1106.8	10.7	3.2	5.3	124.2	3.5	132.1	4.0	147		
ESO 443-042	2815.8	24.8	8.7	9.6			118.6	14.9	119		
ESO 512-012	3313.4	19.0	13.0	6.5			122.8	12.4	123		

^{a} Mean radial velocity (in km s^{-1}). ^{b} Maximum rotational velocity (see the text). ^{c} Central velocity dispersion. ^{d} Mean velocity dispersion. ^{e} Maximum velocity dispersion (see the text). ^{f} References are: (1) Average value quoted in HYPERLEDA; (2) Bottema et al. (1991); (3) Di Nella et al. (1995), and (4) Falcón-Barroso et al. (2002).

5. Dynamical parameters

Radial velocities and velocity dispersions for each spectrum along the bulge radii were measured using a dedicated program within RED$_{m}^{uc}$E, which incorporates the MOVEL and OPTEMA algorithms devised by González (1993). The MOVEL procedure is a refined version of the classic Fourier quotient method (Sargent et al. 1977). The basic improvement over the standard procedure is that, starting from a first guess of γ (mean line-strength), V (radial velocity), and σ (velocity dispersion), it creates a model galaxy that is processed in parallel to the galaxy spectrum. The differences between the input and output parameters of the model spectrum are then used to correct the galaxy power spectrum from systematic effects in the handling of data in the Fourier space. The OPTEMA algorithm allowed us to overcome the typical template mismatch problem. In order to do this, a number of stellar spectra of different spectral types and luminosity classes is fed into the program. In our case, we combined our template stars to construct representative input spectra of the following types: A3-5V, G0-2V, G5V, K0-1V, G8-K0III, K3III, K5-7III, and M3III. The algorithm then constructs an optimal template as a linear combination of the above template spectra, which minimizes the residuals between the galaxy spectrum and the broadened template. Meanwhile, the dynamical parameters are derived as part of the same minimization process. Our tests showed that if a single template star is used to measure the velocity dispersion (instead of the above combination), systematic errors as large as 10% can be introduced.

Figure 2 illustrates the result of this procedure for two galaxies (NGC 7332 and UGC 10043), showing, in the upper panels, the fits between the observed central spectra of the galaxies and the corresponding optimal templates corrected with the derived dynamical parameters. The lower panels show the residual of the fits. Note that emission lines, although almost hidden in the original spectrum (like the [O III]λ5007 line for NGC 7332) are clearly detected after subtracting the template. (Once an emission line is detected, the corresponding wavelength region is not used for minimizing the residuals.) In fact, the optimal templates derived for each galaxy were later used to mask the regions possibly containing emission lines.

Realistic errors in the derived parameters (radial velocity and velocity dispersion) were computed by performing Monte-Carlo simulations, repeating the whole process (including the derivation of the optimal template) for a large number of simulated galaxy spectra created using the error spectrum obtained during the reduction process. We checked that, in order to measure velocity dispersion of the order of the spectral resolution ($\sim$100 km s^{-1} for runs 1, 2, 4, and 5) with a relative error below 20%, we needed spectra with S/N (per Å) greater than 15. This coincides with the cutoff value for the spectral extraction to measure the atomic indices.

Once an optimal template is derived for the central or maximum S/N (if the center is affected by dust lanes) spectrum, the
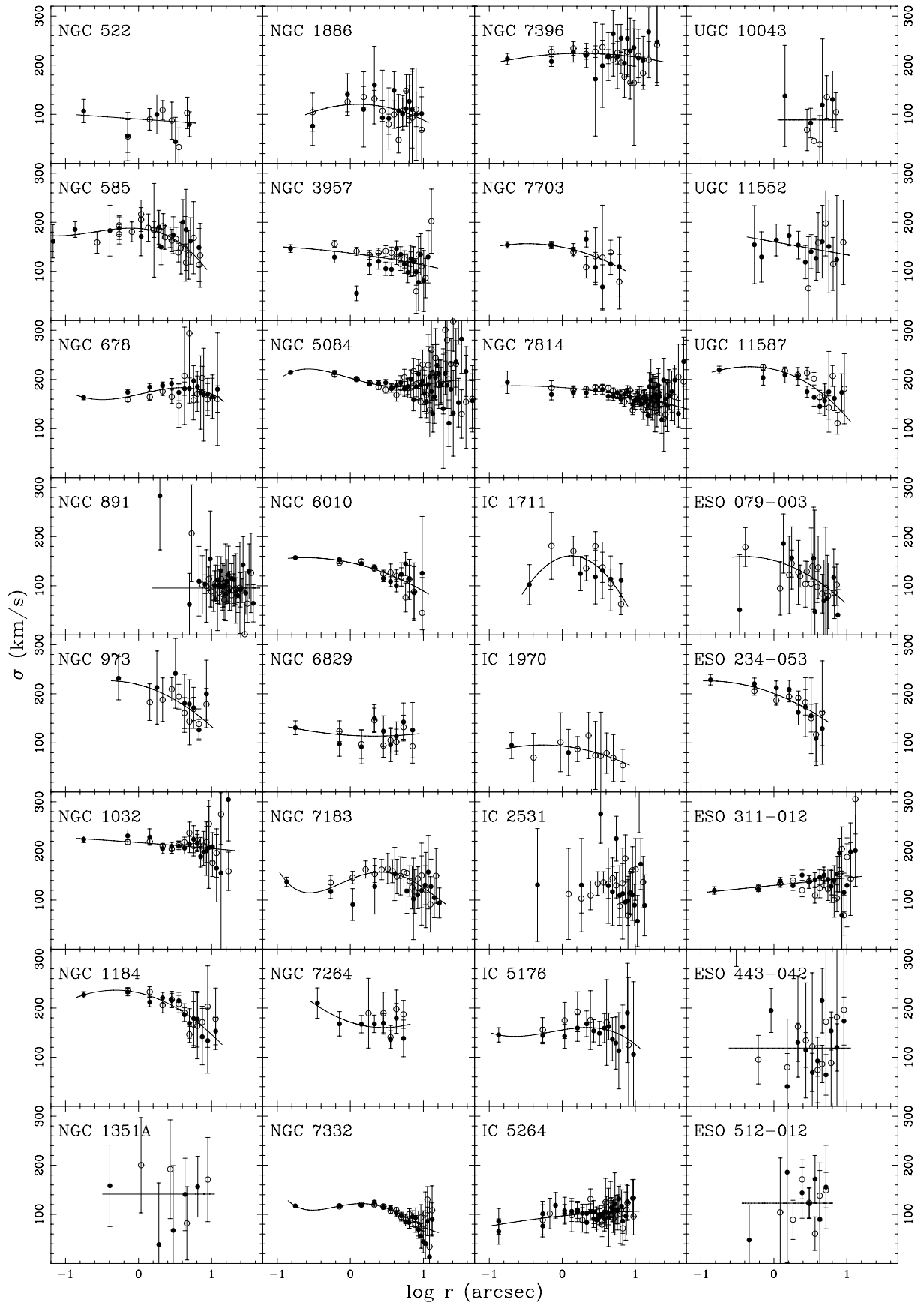
Fig. 3. Velocity dispersion profiles for the galaxy sample. Filled and open symbols refer to spectra of the bulges at either side of the galaxy centers. The plotted lines represent polynomial fits to the profiles. See text for details.

procedure is repeated for all the spectra along the bulge radii, deriving radial profiles for the radial velocity and velocity dispersion. Note that the template derived for the central spectrum is used for the analysis of the rest of the spectra and, therefore, that we are not taking the possible effect of population gradients in the derived sigma profiles into account. However, we preferred to introduce this small inaccuracy over artificially increasing the scatter of the parameters profiles due to unreal changes in the derived linear combinations of templates at each radius. Note also that any radial change in mean line-strength (i.e. γ) or continuum shape is properly corrected from with the MOVEL algorithm.

The dynamical parameters and their corresponding errors at each galactocentric radius are listed in Table 3. Since the slit was oriented along the minor axes of the bulges, no rotation along the slit was expected. To check this, we include the maximum rotational velocity in Table 3 (computed as an error-weighted mean of the, generally two, spectra on each side of the galaxy center with the highest rotational velocity) and its error. It is apparent from the table that most bulges do not show any significant rotation along the minor axes. For some galaxies, however, we observed some hints of rotation or peculiar V_r profiles in the central regions, probably due to slight misalignments of the slit with respect to the minor axis direction or the bulge center.

For galaxies with no obvious dust lanes in the central regions, the table also includes the central velocity dispersion σ_0, measured in an aperture of 4 arcsec times the slit width centered on the galaxy center. We also list mean velocity dispersions ($\langle\sigma\rangle$) defined as the error-weighted mean velocity dispersion of all the extracted spectra along the radius (which is very close to the velocity dispersion that is derived when adding all the spectra along the slit).

The derived velocity dispersion profiles for the galaxy sample are plotted in Fig. 3. Typically, the velocity dispersion decreases with galactocentric radius, although there are different behaviors and some galaxies exhibit a large scatter. It should be noted that the main motivation for measuring velocity dispersion profiles in this paper is to have the necessary information to carry out accurate corrections to the Lick/IDS indices (detailed below). Since line-strength indices depend on the spectral resolution, all spectra along the slit must be corrected to the same velocity dispersion before measuring the indices in order to avoid the introduction of spurious line-strength gradients. However, if we were to use the nominal velocity dispersion values obtained for each individual spectrum to perform this correction, the errors associated with the σ measurement would be introduced into the measured indices. To avoid this, we smoothed the velocity dispersion profiles by fitting low-order polynomials to the data, and we used the predictions of these polynomials for correcting the indices to the desired velocity dispersions. Note that we are not pretending to assign any physical meaning to these polynomial radial profiles; they only serve a calibration purpose. The column $\sigma_{\max}$ in Table 3 gives the maximum velocity dispersion indicated by the polynomials in the observed radial range.

Finally, we compared the derived values with the available data from the literature (last columns of Table 3) to check for any systematic offset in the derived velocity dispersion. To minimize aperture differences, these reference data should be compared with our central (σ_0) values when available, or else with $\langle\sigma\rangle$. It can be seen that we do not have any systematic offset relative to the scarce previous data.

Table 4. Coefficients of the polynomials to correct Lick indices for broadening effects.

Index	c_1	c_2	c_3
$H\delta_A$	0.76129	0.10120	0.13751
$H\delta_F$	1.25993	−0.51501	0.25508
CN_1	0.70442	0.31941	−0.02382
CN_2	0.76492	−0.00441	0.23949
Ca4227	0.78022	−0.28090	0.50067
G4300	0.89152	0.10002	0.00847
$H\gamma_A$	1.11845	−0.21248	0.09403
$H\gamma_F$	0.80429	0.25651	−0.06080
Fe4383	0.87985	−0.00952	0.12967
Ca4455	0.63849	0.09619	0.26532
Fe4531	0.91332	−0.01235	0.09903
Fe4668	1.00545	−0.12685	0.12140
$H\beta$	0.99068	0.00563	0.00369
Fe5015	0.78157	0.17915	0.03928
Mg_1	0.97728	0.01066	0.01206
Mg_2	0.98082	0.02199	−0.00282
Mgb	0.96450	−0.07495	0.11045
Fe5270	0.82533	0.12283	0.05184
Fe5335	0.84324	−0.08141	0.23817
Fe5406	0.89017	−0.14121	0.25104
Fe5709	0.89437	0.01365	0.09198
Fe5782	0.86475	−0.14458	0.27983
Na5895	0.94445	0.01617	0.03938
TiO_1	1.00000	0.00000	0.00000
TiO_2	1.00000	0.00000	0.00000

6. Line-strength indices

Line-strength indices in the Lick/IDS system (e.g. Worthey et al. 1994; Worthey & Ottaviani 1997) were measured for all the extracted spectra along the measured extent of the bulge. We measured all the indices from $H\delta$ to Fe5406. In the case of runs 4 and 5 (cf. Table 2), the extended spectral range allowed us to also include the redder Lick indices (up to the TiO indices). The next sections explain all the procedures to derive reliable errors in the line-strengths and to transform them to the spectrophotometric Lick/IDS system. All these steps were possible thanks to including a number of stars from the Lick/IDS library in the different observing runs. In particular, we observed 40, 40, 19, 4, and 6 Lick standard stars (covering a range of spectral types and luminosity classes) in runs from 1 to 5, respectively.

6.1. Error analysis

A first estimation of errors in the line strengths was accomplished by taking three different error sources into account: *(i)* photon noise (the errors were calculated using the variance spectra computed as part of the reduction process); *(ii)* flux calibration (the estimation was based on the comparison of the indices measured using the different flux calibration curves obtained in each observing run); and *(iii)* uncertainties in the wavelength scale (due to errors in the wavelength calibration and in the measurement of the radial velocity). Except for the spectra with the highest S/N, the dominant error source was the first one.

To check and refine the error analysis, we analyzed the line strengths obtained for *(i)* repeated observations of the same stars within each observing run, *(ii)* stars in common among different observing runs (e.g. all the 40 Lick stars observed in run 1 were repeated in run 2), and *(iii)* separate observations of the same galaxies within each run. (Typically the observation of a galaxy was split into 4–12 different exposures.) Using this

Table 5. Spectral resolutions, residual errors, and offsets needed to transform line-strength indices to the Lick/IDS system.

| Index | σ_L^a | Residual errors | | | | Offsets | | | | σ^b | |
	km s^{-1}	run 1	run 2	run 3	runs 4, 5	run 1	run 2	run 3	runs 4, 5	rms	exp
Hδ_A	325	0.00	0.00	0.00	0.20	−0.34	−0.34	0.00	−1.09	0.66	0.37
Hδ_F	325	0.00	0.00	0.00	0.00	−0.12	−0.09	0.00	−0.81	0.35	0.24
CN$_1$	325	0.005	0.005	0.005	0.008	+0.003	+0.003	−0.009	0.000	0.020	0.015
CN$_2$	325	0.004	0.004	0.004	0.011	+0.008	+0.008	−0.015	−0.011	0.021	0.016
Ca4227	300	0.04	0.04	0.04	0.00	0.00	0.00	−0.08	0.00	0.23	0.17
G4300	300	0.13	0.13	0.13	0.00	−0.08	−0.08	0.00	0.00	0.38	0.32
Hγ_A	275	0.19	0.19	0.21	0.00	+0.41	+0.41	+0.41	+0.34	0.48	0.40
Hγ_F	275	0.04	0.00	0.00	0.00	+0.17	+0.17	0.00	+0.10	0.22	0.19
Fe4383	250	0.22	0.21	0.21	0.09	+0.08	+0.08	0.00	−0.36	0.53	0.45
Ca4455	250	0.04	0.04	0.04	0.00	+0.32	+0.32	0.00	+0.28	0.20	0.20
Fe4531	250	0.10	0.10	0.10	0.18	+0.15	+0.15	−0.32	0.00	0.35	0.31
Fe4668	250	0.15	0.19	0.15	0.57	0.00	0.00	−1.03	0.00	0.57	0.59
Hβ	225	0.10	0.10	0.10	0.04	−0.07	−0.07	0.00	−0.14	0.22	0.20
Fe5015	200	0.15	0.19	0.15	0.21	+0.26	+0.26	−0.11	0.00	0.64	0.40
Mg$_1$	200	0.004	0.004	0.004	0.007	+0.011	+0.003	+0.016	+0.009	0.011	0.010
Mg$_2$	200	0.006	0.005	0.003	0.005	+0.025	+0.020	+0.021	+0.016	0.012	0.010
Mgb	200	0.04	0.03	0.02	0.07	0.00	0.00	−0.08	0.00	0.31	0.17
Fe5270	200	0.00	0.00	0.00	0.11	0.00	+0.03	0.00	0.00	0.23	0.16
Fe5335	200	0.02	0.02	0.02	0.16	−0.06	−0.06	0.00	+0.18	0.26	0.16
Fe5406	200	0.04	0.04	0.04	0.03	−0.04	−0.04	−0.19	0.00	0.23	0.14
Fe5709	200				0.00				−0.08	0.14	0.14
Fe5782	200				0.00				+0.14	0.10	0.13
Na5895	200				0.24				0.00	0.26	0.40
TiO$_1$	200				0.003				+0.013	0.008	0.007
TiO$_2$	200				0.000				−0.015	0.005	0.004

^{a} Spectral resolutions at which line-strength indices should be measured to roughly match the original Lick/IDS system. ^{b} Measured (rms) and expected (exp) standard deviations for the comparison of indices with the original values of the Lick/IDS system.

data, we computed residual errors as the quadratic differences between the measured rms dispersions and the expected total error from the three sources of uncertainty quoted in the previous paragraph. The resulting residual errors are listed in Table 5 for each index and observing run. They are relatively modest but were included anyway in the final uncertainties.

6.2. Emission-line corrections

Some line-strength indices, in particular Hβ, Fe5015, and Mgb, are potentially affected by emission lines (e.g., Goudfrooij & Emsellem 1996). Most of our galaxies exhibit non-negligible nebular emission, as judged from their [O III]λ5007 line. Usually, the emission is concentrated towards the bulge centers, where the spectra are heavily contaminated by the disk light (H II regions can project onto the slit). However, in some special cases (e.g., NGC 1886 and NGC 7332), line emission can even be detected in the outer part of the bulge, where any contamination by disk light is negligible. For instance, in NGC 7332, the line emission increases to EW([O III]λ5007) $\simeq$ 4 Å at a distance of ∼16 arcsec from the center.

The correction of Hβ from the emission contribution is a troublesome task. The usual procedure (see eg. González 1993; Trager et al. 2000) relies on using the equivalent width of [O III] to apply an empirical correction. In this paper, given the uncertainties of that correction and the fact that the emission is relatively strong for many of the galaxies, we have decided not to correct Hβ and, therefore, not to use it in our analysis in the cases where any [O III]λ5007 emission was detected (in particular when its measured equivalent width was larger than its error).

We determined equivalent widths of [O III]λ5007 after subtracting from each galaxy spectrum an emission-free template

spectrum constructed from the broadened optimal template derived for that galaxy during the velocity dispersion measurement (see Fig. 2). In order to measure the Fe5015 and Mgb indices in spectra with emission lines, we masked the spectral regions affected by the [O III]λ4959, [O III]λ5007, and [N I]λ5199 lines and replaced them with the corresponding regions in the broadened optimal template spectrum.

6.3. Broadening corrections

As mentioned before in Sect. 5, the Lick/IDS indices have to be corrected for spectral broadening. In order to avoid the introduction of artificial line-strength gradients due to changes in velocity dispersion along the slit, we broadened all the spectra of a given galaxy to match the maximum velocity dispersion σ_{max} derived in Sect. 5 by convolving it with a Gaussian of width $(\sigma_{max}^2 - \sigma_r^2)^{1/2}$, where σ_r is the velocity dispersion at each radius predicted by the corresponding polynomial fit.

The conversion of the line indices to the resolution of the Lick system (see Sect. 6.4) was done as follows. In the cases where the total resolution of the spectra (the quadratic sum of instrumental resolution and the maximum velocity dispersion for the galaxy) was below the Lick resolution, we simply broadened the spectra by the quadratic difference. In other cases, we applied an empirical correction to the measured indices. This correction was derived by broadening stellar spectra by convolution with Gaussians having a range of σ values. Since this correction depends on the individual spectral type of the star, we instead used the optimal templates obtained in the velocity dispersion measurement procedure to derive the following expression:

$$I(\sigma_0) = I(\sigma)\left(c_1 + c_2\,\sigma/\sigma_0 + c_3\,(\sigma/\sigma_0)^2\right), \quad (1)$$
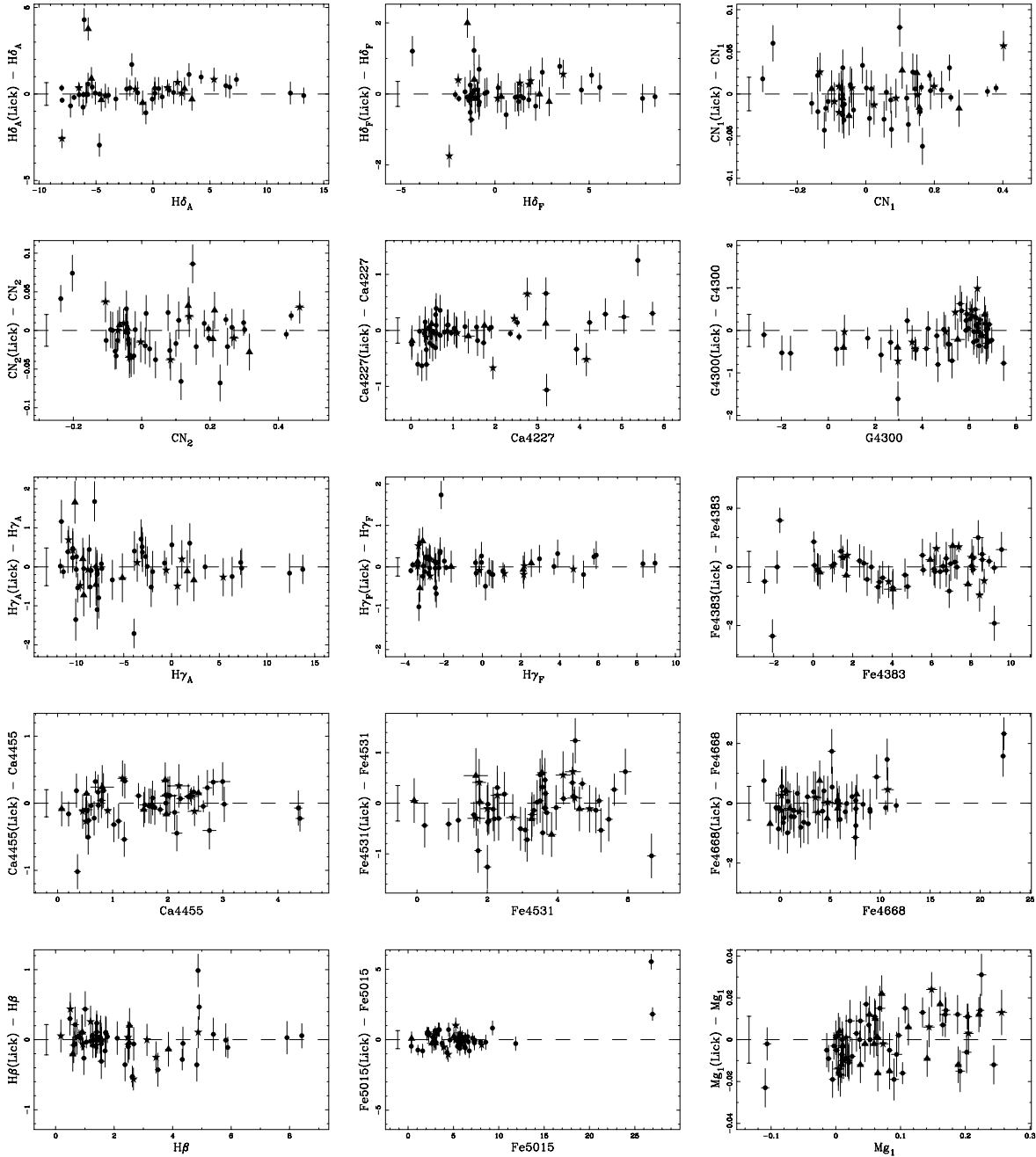
Fig. 4. Comparison of the line-strength indices in the Lick/IDS spectra and the measurements in our sample of stars after correcting to the Lick/IDS system. Different symbols refer to the different observing runs, using the following code: circles for runs 1 and 2, triangles for run 3, and stars for runs 4 and 5. In the case of the TiO indices, both TiO_1 are TiO_2 are plotted in the same panel, using closed and open symbols for both indices, respectively. The length of the error bar near the left end of each panel is twice the rms standard deviation of each dataset with respect to the zero offset horizontal line.

which can be used to convert an index I measured at a resolution σ to any other resolution σ_0. The values of the c_i coefficients are listed in Table 4 for all the Lick indices. In principle, the exact values of the coefficients depend on the particular optimal template used. However, the spectral differences among them have a weak effect on the derived polynomials and the uncertainties introduced by using the listed mean coefficients are well below the other sources of errors.

6.4. Conversion to the Lick/IDS system

Transformation of line strengths to the Lick/IDS system is not straightforward. Basically, there are two important effects that

have to be taken into account. First, the Lick/IDS spectra are not flux-calibrated using a spectrophotometric standard star, but by using a normalized tungsten lamp spectrum. Thus, there are significant differences in the spectral shapes when compared with flux-calibrated spectra. This effect causes systematic offsets, especially for indices with broad bands like (e.g.) Mg_2. Second, the spectral resolution of the Lick spectra is not constant with wavelength, in particular it degrades considerably towards the blue end. This has an important effect on narrow-line indices, like many of the atomic ones. For a comprehensive discussion of these effects, we refer the reader to Worthey & Ottaviani (1997).

To transform our data to the Lick/IDS system, we performed the following steps. First, we estimated the resolution at which
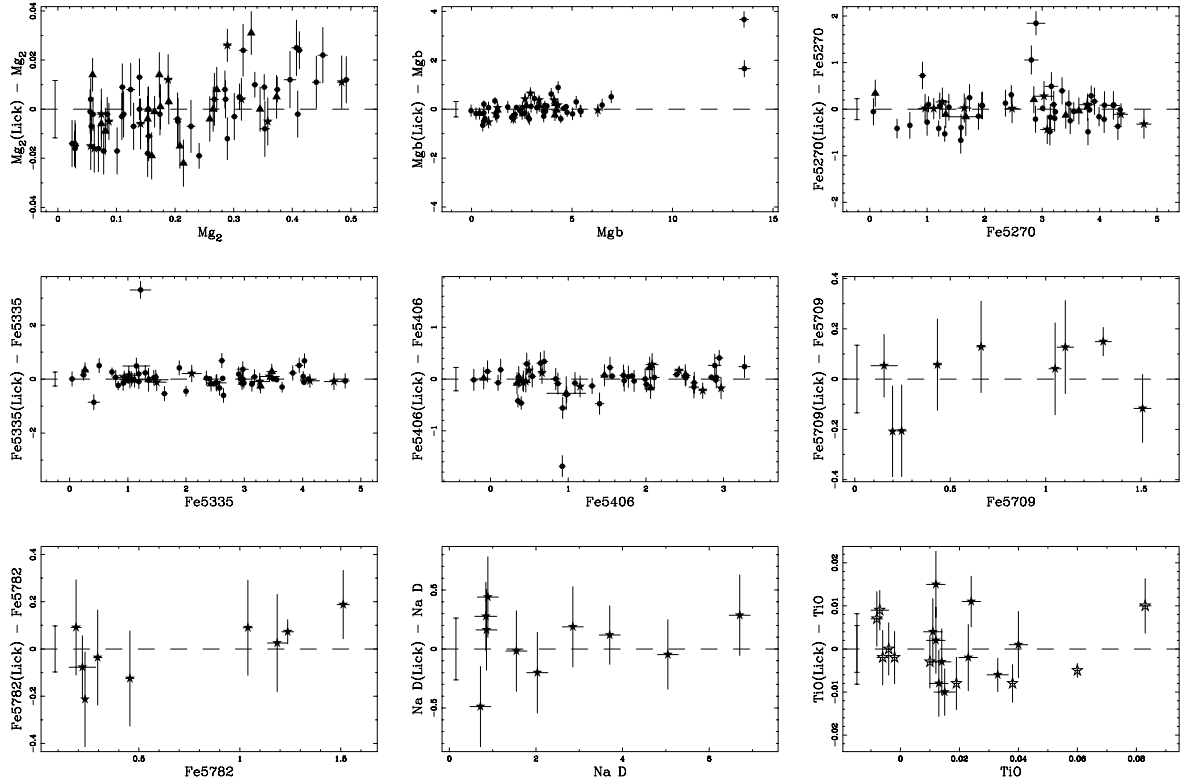
Fig. 4. continued.

each particular index should be measured by broadening our large set of stars in common with the Lick library to several line widths, in steps of 25 km s^{-1}. We did not attempt to find precise resolutions for each index since these depend on the particular set of stars being used. Instead, we estimated the approximate line widths σ_L which, changing softly with wavelength, minimized the residuals. These are given, for each index, in the second column of Table 5. These resolutions agree with the rough estimates given in Worthey & Ottaviani (1997).

We then broadened all our stellar spectra to the above σ_L resolutions and measured the line-strength indices. The comparison of these measurements with those in the original Lick/IDS spectra allowed us to derive mean offsets for all the indices in each observing run. These additive offsets, listed in Table 5, are mainly due to differences in flux calibration between both systems, but also include a fine tuning of the broadening corrections and systematic effects in both our data (like uncertainties in the spectral resolution or flux calibration) and the Lick/IDS data (like spectral peculiarities that depend on the particular Lick/IDS run in which each star was observed). Note that we obtain different offsets for each observing run (although in most cases they are similar). In fact, the comparison with Lick data provides us with an anchor system to correct for small offsets among the different runs. It must be noted that the offsets for run 3, with a significantly lower spectral resolution, are of the same order as the offsets for the other runs, which confirms that the broadening corrections have been properly done.

Figure 4 shows a comparison of the line-strength indices in the Lick/IDS spectra and the measurements in our sample of stars after correcting to the Lick/IDS system. Error bars were derived by combining the computed errors for our measurements and the errors of the original Lick/IDS indices as taken from Worthey et al. (1994). The last two columns of Table 5 give the rms standard deviation with respect to the zero offset and the standard deviation that should be expected from the computed

errors in the offsets. As can be seen, the former are usually larger than the latter, indicating that the errors in the I(Lick) $- I$(here) differences are somewhat underestimated. Given all the tests that we have carried out with our data, we think that this disagreement is most likely due to an underestimate of the errors in the original Lick measurements.

6.5. Final data

Once all the previous corrections had been derived, we applied them to the extracted spectra along the bulge radii and measured the line strengths. We derived two sets of final data:

1. In the first one, we introduced the residual errors, masked the emission lines, converted all the indices to a resolution corresponding to the maximum velocity dispersion along the radius (as listed in Table 3), and applied relative offsets among runs to put them in the same spectrophotometric system (which should be very close to a true flux-calibrated system). To do this, we applied the offsets listed in Table 5 with respect to run 2. (Offsets for run 2 were therefore zero.) However, we did not transform the indices to the Lick/IDS system. This data can be very useful for future studies working at any spectral resolution and in a flux-calibrated system. Note that, in this dataset, indices from different galaxies cannot be compared directly, since indices are measured at different resolutions.
2. For the second dataset, we carried out a full transformation to the Lick/IDS system, applying (in addition to the corrections from the last paragraph) the necessary offsets and the index-dependent velocity dispersion corrections. For this last step, we broadened the spectra when possible or applied the polynomials of Table 4 when the original resolutions (the quadratic sum of σ_{max} and the instrumental resolution) were higher than σ_L (Table 5).
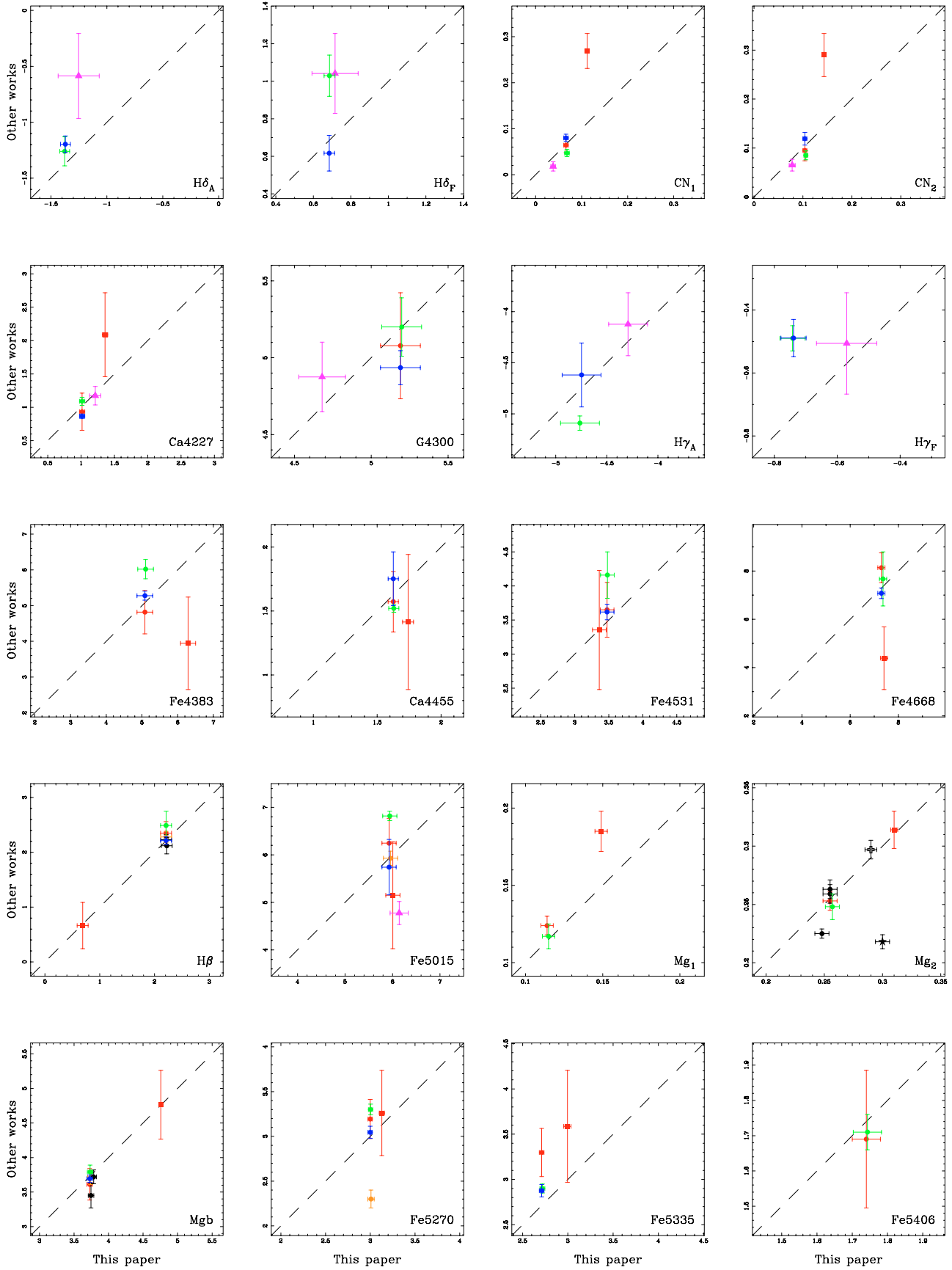
Fig. 5. Comparison of the line-strength indices measured in the central regions with data from other workers. Different symbols are used for different galaxies: squares for NGC 5084, crosses for NGC 6010, triangles for NGC 7703, circles for NGC 7332, and stars for NGC 7814. Color codes refer to data from Trager et al. (1998) (red), Sánchez-Blázquez et al. (2006) (blue), Caldwell et al. (2003) (magenta), Kuntschner et al. (2007) (orange), Denicoló et al. (2005) (green), and other sources (black).

6.6. Comparison with other works

Finally, in Fig. 5 we present a comparison of the line-strengths measured in the central regions of our bulges with the available results from the literature. The galaxies with existing published data and the corresponding references are the following: NGC 5084 (Trager et al. 1998), NGC 6010 (Falcón-Barroso et al. 2002), NGC 7703 (Caldwell et al. 2003), NGC 7332 (Bender et al. 1993; Trager et al. 1998; Golev et al. 1999; Falcón-Barroso et al. 2002, 2004; Denicoló et al. 2005; Sil'chenko 2006; Kuntschner et al. 2006; Sánchez-Blázquez et al. 2006b), and NGC 7814 (Prugniel et al. 2001). To perform the comparison for each galaxy and reference, we binned our spectra in the central regions of the bulges to reproduce the aperture used by the corresponding works as closely as possible. It is apparent from the figure that, although there is general agreement with the data from other workers, there are also some important discrepancies for some particular line strengths and authors (like some indices for NGC 5084 from Trager et al. 1998, or the Mg_2 measurement for NGC 7814). These differences could be due to: low S/N ratios in the spectra of other authors, variations in the centering of the slit or in the observed aperture, or differences in the calibration and data reduction processes. However, the fact that, when there are several published values for a galaxy (NGC 7332), our measurements agree with the majority of them gives us confidence in our measured values. For instance, for the 5 previous measurements for the central Mg_2 index in NGC 7332, our value agrees with 4 out of them within the errors.

The comparison with the central line-strengths from Sánchez-Blázquez et al. (2006b) is of particular relevance, since in Paper II we will make use of this dataset as a comparison sample of elliptical galaxies. In this case, we plot the indices measured in an aperture of 2×4 arcsec (as listed in Sánchez-Blázquez 2004), finding good agreement with our data (with the exception of the $H\gamma_F$ index, although note that the results agree for $H\gamma_A$).

7. Summary

We have introduced our long-term project devoted to understanding the evolutionary status of galaxy bulges by presenting the sample and the most relevant details of our survey of long-slit spectra along the minor axis of bulges in edge-on spiral galaxies. After summarizing a data reduction process characterized by a very detailed error analysis, we have presented our procedures to measure dynamical parameters and all the Lick/IDS line-strength indices available in the spectra. A special emphasis was made in the broadening corrections of the indices and their conversion to the Lick/IDS system. As a final product, we derived tables giving all the parameters (radial velocities, velocity dispersions, and indices) at each galactocentric radius for all the bulges in the sample. In the case of the indices, two datasets have been obtained: one with the indices in flux-calibrated spectra and at the *natural* resolution of the bulges (i.e. internal plus instrumental), and another in which all the indices have been converted to the Lick/IDS system. These two datasets will be available in electronic form at CDS.

In the next paper of this series we will measure line-strength gradients and analyze them in the light of different galaxy formation scenarios.

References

Andredakis, Y. C., Peletier, R. F., & Balcells, M. 1995, MNRAS, 275, 874
Arimoto, N., & Jablonka, P. 1991, A&A, 249, 374
Balcells, M., & Peletier, R. F. 1994, AJ, 107, 135
Balcells, M., Graham, A. W., Domínguez-Palmero, L., & Peletier, R. F. 2003, ApJ, 582, L79
Bekki, K., & Shioya, Y. 1999, ApJ, 513, 108
Bender, R., Burstein, D., & Faber, S. M. 1992, ApJ, 399, 462
Bender, R., Burstein, D., & Faber, S. M. 1993, ApJ, 411, 153
Bottema, R., van der Kruit, P. C., & Valentijn, E. A. 1991, A&A, 247, 357
Caldwell, N., Rose, J. A., & Concannon, K. D. 2003, AJ, 125, 2891
Cardiel, N. 1999, Ph.D. Thesis, Universidad Complutense de Madrid
Cardiel, N., Gorgas, J., & Aragón-Salamanca, A. 1995, MNRAS, 277,502
Cardiel, N., Gorgas, J., Cenarro, A. J., & González, J. J. 1998, A&AS, 127, 597
Carlberg, R. G. 1984, ApJ, 286, 403
Carollo, C. M., Danziger, I. J., & Buson, L. M. 1993, MNRAS, 265, 553
Courteau, S., de Jong, R. S., & Broeils, A. H. 1996, ApJ, 457, L73
de Jong, R. S., Simard, L., Davies, R. L., et al. 2004, MNRAS, 355, 1155
Denicoló, G., Terlevich, R., Terlevich, E., et al. 2005, MNRAS, 356, 1440
di Nella, H., García, A. M., Garnier R., & Paturel, G. 1995, A&AS, 113, 151
Falcón-Barroso, J., Peletier, R. F., & Balcells, M. 2002, MNRAS, 335, 741
Falcón-Barroso, J., Peletier, R. F., Emsellem, E., et al., 2004, MNRAS, 350, 35
Fisher, D., Franx, M., & Illingworth, G. D. 1996, ApJ, 459, 110
Friedli, D. 1998, in Abundance Profiles: Diagnostic Tools for Galaxy History, ed. D. Friedli et al. (San Francisco: ASP), 287
Friedli, D., & Benz, W. 1995, A&A, 310, 649
Friedli, D., Benz, W., & Kennicutt, R. 1994, ApJ, 430, L105
Golev, V., Prugniel, Ph., Simien, F., & Longhetti, M. 1999, A&AS, 136, 519
González, J. J. 1993, Ph.D. Thesis, University of California, Santa Cruz
González, J. J., & Gorgas, J. 1996, in Fresh Views on Elliptical Galaxies, ed. A. Buzzoni, A. Renzini, & A. Serrano (San Francisco: ASP), 225
Gorgas, J., Jablonka, P., & Goudfrooij, P. 2003, in Highlights of Spanish Astrophysics III, ed. J. Gallego, J. Zamorano, & N. Cardiel (The Netherlands: Kluwer Academic Pub.), 99
Goudfrooij, P., & Emsellem, E. 1996, A&A, 306, L45
Goudfrooij, P., Gorgas, J., & Jablonka, P. 1999, Ap&SS, 269, 109
Hamuy, M., Suntzeff, N. B., Heathcote, S. R., et al. 1994, PASP, 106, 566
Idiart, T.P., de Freitas Pacheco, J. A., & Costa, R. D. D. 1996, AJ, 112, 2541
Jablonka, P., Martin, P., & Arimoto, N. 1996, AJ, 112, 1415
Jablonka, P., Gorgas, J., & Goudfrooij, P. 2002, Ap&SS, 281, 367
Kauffmann, G., White, S. D. M., & Guiderdoni, B. 1993, MNRAS, 264, 201
Kormendy, J., & Kennicutt, R. C. 2004, ARA&A, 42, 603
Kuntschner, H., Emsellem, E., Bacon, R., et al. 2006, MNRAS, 369, 497
Lauberts, A. 1982, The ESO/Uppsala survey of the ESO(B) atlas
Lütticke, R., Dettmar, R.-J., & Pohlen, M. 2000, A&AS, 145, 405
Martin, P., & Roy, J.-R., 1994, ApJ, 426, 601
Massey, P., Strobel, K., Barnes, J. V., & Anderson, E. 1988, ApJ, 328, 315
McArthur, L. A., Courteau, S., & Holtzman, J. A. 2003, ApJ, 582, 689
Mehlert, D., Thomas, D., Saglia, R. P., Bender, R., & Wegner, G. 2003, A&A, 407, 423
Moorthy, B. K., & Holtzman, J. A. 2006, MNRAS, 371, 583
Nilson, P. 1973, Uppsala general catalogue of galaxies, Nova Acta Regiae Societatis Scientiarum Upsaliensis, Ser. V, A, Vol. 1
Norman, C. A., Sellwood, J. A., & Hasan, H. 1996, ApJ, 462, 114
Oke, J. B. 1990, AJ, 99, 1621
Peletier, R. F., Balcells, M., Davies, R. L., et al. 1999, MNRAS, 310, 703
Pfenniger, D., & Norman, C. A. 1990, ApJ, 363, 391
Prugniel, Ph., Maubon, G., & Simien, F. 2001, A&A, 366, 68
Sánchez-Blázquez, P. 2004, Ph. D. Thesis, Universidad Complutense de Madrid
Sánchez-Blázquez, P., Gorgas, J., & Cardiel, N. 2006a, A&A, 457, 823
Sánchez-Blázquez, P., Gorgas, J., Cardiel, N., & González, J. J., 2006b, A&A, 457, 787
Sargent, W. L. W., Schechter, P. L., Boksenberg, A., & Shortridge, K. 1977, ApJ, 212, 326
Sil'chenko, O. K. 2006, ApJ, 641, 229
Trager, S. C., Worthey, G., Faber, S. M., Burstein, D., & González, J. J. 1998, ApJS, 116, 1
Trager, S. C., Faber, S. M., Worthey, G., & González, J. J. 2000, AJ, 119, 1645
Vila-Costas, M. B., & Edmunds, M. G. 1992, MNRAS, 259, 121
Worthey, G., & Ottaviani, D. L. 1997, ApJS, 111, 377
Worthey, G., Faber, S. M., González, J. J., & Burstein, D. 1994, ApJS, 94, 687
Zaritsky, D., Kennicutt, R. C., & Huchra, J. P. 1994, ApJ, 420, 87